# A new experimental setup for time-resolved measurements of interactions between gas jets and flexible surfaces

OPEN ACCESS
IOP Publishing
Measurement Science and Technology
Meas. Sci. Technol. **33** (2022) 125202 (12pp)
https://doi.org/10.1088/1361-6501/ac86e4

# A new experimental setup for time-resolved measurements of interactions between gas jets and flexible surfaces

**Johannes Burkert*** and **Rüdiger Schwarze**

Institute of Mechanics and Fluid Dynamics, TU Bergakademie Freiberg, Lampadiusstr. 4, 09599 Freiberg, Germany

E-mail: johannes.burkert@imfd.tu-freiberg.de

Received 10 February 2022, revised 22 July 2022
Accepted for publication 4 August 2022
Published 5 September 2022

**Abstract**

The purpose of this study was to present a new setup for time-resolved measurements of the interactions between gas jets and flexible surfaces. Such interactions are dominated by characteristic surface deformations and gas-driven surface waves. Previous works have studied the gas–surface interaction only in a sectional plane but not as a three-dimensional problem. In our setup, surface deformations and waves were generated by the impingement of a supersonic jet on a flexible surface made of a silicon membrane. The inlet pressure of the Laval nozzle was varied from 0.8 bar to 3 bar and the nozzle surface distance was set in the range of 30–120 mm with respect to the flat surface. The entire surface area and its behavior were recorded using a high-speed camera. The evaluation was based on the pixel intensity values of the recorded surface images during the jet impingement. A fast Fourier transformation was applied to the results to determine the dominant frequencies of surface movements in detail. From this, low- and high-frequency events on the surface can be derived. Correlations between the main process parameters, nozzle distance, nozzle inlet pressure and characteristic surface behavior were deduced and mapped.

Keywords: jet–surface interactions, flexible surface, jet impingement, gas-driven surface waves, time-resolved measurements

(Some figures may appear in colour only in the online journal)

## 1. Introduction

Gas jet impingement on either solid or liquid surfaces is of great fluid mechanical interest. Here, the interactions especially during supersonic gas jet impingement on solid surfaces are well documented, e.g. in [1–3]. In such situations, only the gas flow field is highly dynamic and the shape of the surface does not change. As the main phenomenon, the so-called feedback loop of the gas jet is well described in the literature, as this acoustic phenomenon initiates two different jet modes known as symmetric and helical. Additional experiments [4] with pressure-sensitive paint revealed a rotation of the supersonic jet around its symmetry axis. The dominant mode depended on the nozzle height above the surface.

However, interactions between gas jets and flexible surfaces occur during gas jet impingement on a liquid pool with a free surface. Such processes are used in steel production

* Author to whom any correspondence should be addressed.



 

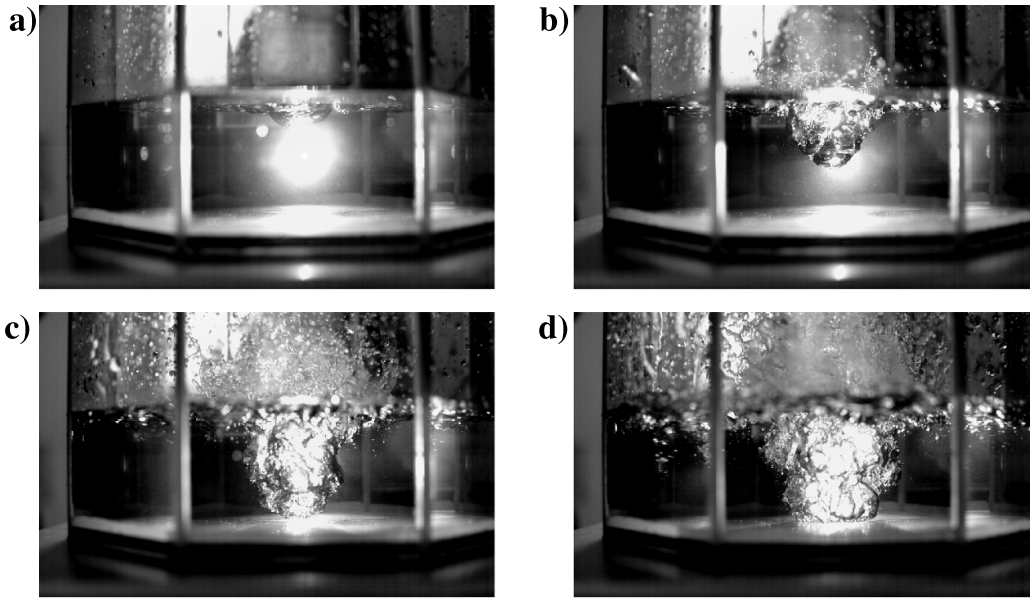


**Figure 1.** Snapshots of initial measurement to visualize the process of jet impinging on a water pool with free surface. The pressure is slowly increased to illustrate the cavity development and onset of droplet separation and deposition and splashing.

(basic oxygen furnace) [5], painting (spray applications) [6], aerospace (vertical take-off and landing vehicles) [7] and medicine (treatment of bio-liquids with atmospheric plasma jets) [8].

In these configurations, the flexible free surface is deformed under the action of an impinging gas jet. The first fundamental characterization of these interactions for jet impingement on a liquid pool is given in [9]. The authors investigated the influence of different parameters, such as nozzle height $h_n$, that is, the nozzle surface distance with respect to the flat surface, nozzle diameter $d_n$, gas flow rate $Q$, pool diameter $d_F$ and liquid level $h_F$ in the pool on the deformation of the free surface of the liquid. They found an empirical correlation between these parameters and the cavity shape, formed by the gas jet in the liquid pool.

The free surface deformation, especially the cavity shape and behavior, has been the focus of further studies, for example, [10–12], or [5]. Typically, optical observations of the surface deformation and behavior from a side view have been employed to analyze the general cavity shape and surface oscillations. Based on this approach, different modes of surface deformation, such as dimpling, splashing, and penetration, have been introduced [13]. It was also found that gas–surface interactions may exhibits strong fluctuations or oscillations [8].

However, the free surface is observed in the side view only as a contact line between the liquid and the gas. Therefore, this approach inadequately captures the jet–surface interactions, behavior of the cavity, and surface waves owing to the limitations of optical access. Accordingly, a more detailed understanding of the fluid mechanics and three-dimensional (3D) behavior of the flexible surface under the action of an impinging jet is still lacking.

Such time-resolved, 3D simultaneous measurements of cavity behavior and free surface waves are difficult to perform especially in the case of gas jet impingement on a liquid pool. As an example, figure 1 illustrates this process with different secondary phenomena, such as splashing, droplet separation, spray formation, surface waves, cavity oscillation, etc taking place simultaneously. Therefore, the focus of the present work is to introduce an optical noninvasive method to perform time-resolved measurements of a completely flexible surface during gas-jet impingement. Both deep-surface deformation and surface-wave propagation were studied in detail. To the best of our knowledge, we are not aware of such an attempt in the literature.

To test our setup, an elastic membrane of 100 µm thickness attached to the edge of an air-filled reservoir represents the flexible surface and mimics a free liquid surface. The membrane suppresses interfering phenomena of secondary importance, such as droplet separation, splashing, and foaming. Therefore, the simultaneous observation of cavity and surface waves is much easier, and the methods used can be tested more rigorously. In advance, we carried out measurements with a membrane stretched over the water-filled pool. However, these preliminary tests showed that the combination of the membrane attached to the water surface is much stiffer than the free water surface and surface structures on the membrane were completely damped out.

## 2. Material and methods

### 2.1. Experimental setup

The test rig illustrated in figures 2(a) and (b) was designed to enable time-resolved measurements of the overall surface behavior with surface deformation, deep cavity formation, and surface waves. The gas flow field in the jet and back-flow regions can be investigated using a schlieren imaging setup.

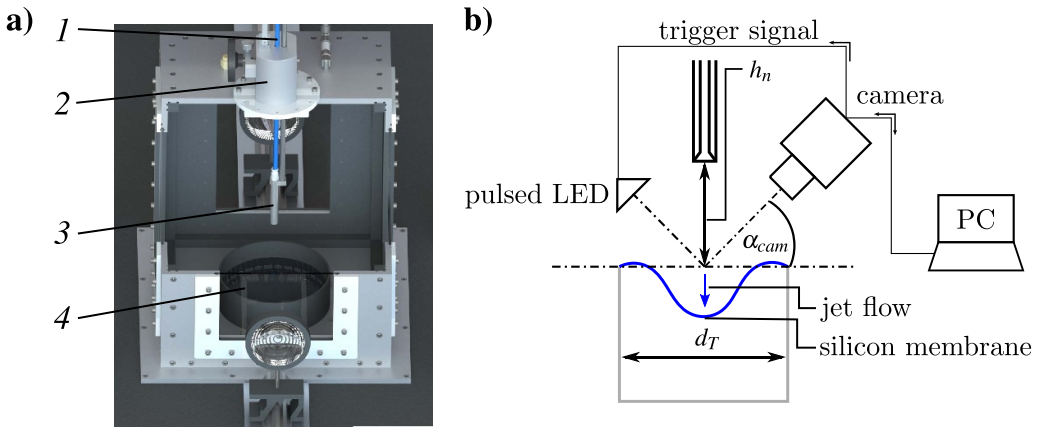


**Figure 2.** (a) CAD rendering of the process chamber with (1) pressurized air supply, (2) nozzle lifting unit, (3) nozzle, (4) fluid reservoir. (b) Setup of the silicone membrane impinging experiments.

However, the latter falls within the scope of future work and will not be described further here.

The process chamber had four transparent windows for optical access and provided a complete view of the flexible surface. Please note, that the liquid surface is replaced by a flexible membrane and there is no liquid, but only air in the pool below the membrane. In this context, it is clear that some effects that characterize the free liquid surface behavior are not correctly captured in this method. However, the scope of the present study is to test the measurement principle for the detection of the characteristic structures as well as frequencies. The complex physical interactions between surface and gas jet will be examined in a subsequent study. We operate the test rig with pressurized air from the laboratory supply, which is adjustable from $p_0 = 0.2\,\mathrm{bar}$ to $p_0 = 8\,\mathrm{bar}$. To prevent pressure oscillations, a pressure regulator valve with an internal damping function was used.

The nozzle height $h_\mathrm{n}$ can be varied by using a rack with a 1 mm slope in the range of 10–200 mm. In addition, the critical diameter of the nozzle was $d_\mathrm{n} = 3\,\mathrm{mm}$ to ensure supersonic flow for operating pressures above $p_0 = 1.5\,\mathrm{bar}$. The reservoir diameter is $d_\mathrm{T} = 200\,\mathrm{mm}$, and the modeled liquid level $h_\mathrm{F} = 100\,\mathrm{mm}$ was equal to the distance between the membrane and the reservoir bottom and corresponded to a complete filling of the reservoir. The flexible membrane is made off silicon, has a thickness of 100 µm and is clamped to the edge of the reservoir. The material parameters are as follows: density $\rho_\mathrm{M} = 1155\,\mathrm{kg\,m^{-3}}$, tensile strength $\sigma_\mathrm{M} = 13.8\,\mathrm{N\,mm^{-2}}$ and bending stiffness $K_\mathrm{M} = 10.9 \times 10^{-2}\,\mathrm{N\,mm^{-2}}$. These parameters are provided by the manufacturer FILK (FILK—Forschungsinstitut für Leder und Kunststoffbahnen in Freiberg, Germany). At this point we would like to point out that the membrane is only used to verify the measurement method. The material behavior of the membrane is not of interest.

With these parameters, we introduce the following dimensionless parameters

$$h_\mathrm{n}^* = \frac{h_\mathrm{n}}{d_\mathrm{n}}\,, \qquad p_0^* = \frac{p_0}{p_\mathrm{amb}} \tag{1}$$

where $h_\mathrm{n}^*$ is the dimensionless nozzle height and $p_0^*$ is the dimensionless inlet pressure normalized to the ambient pressure, $p_\mathrm{amb} = 1.013\,\mathrm{bar}$. Figure 2(b) shows a sketch of the measurement arrangement. A Phantom V12 high-speed camera (resolution of $1280 \times 800\,\mathrm{px}$) was used to observe the scene at an angle of $\alpha_\mathrm{cam} = 45°$. A pulsed LED ring-light illuminated the surface completely and homogeneously. This setup enables a wide variety of sample frequencies from low to high-speed measurements. In the upcoming section, a sampling frequency of $f_\mathrm{S} = 1000\,\mathrm{Hz}$ enabled time-resolved measurements of the surface behavior.

### 2.2. Data procession

The images were processed as shown in figures 3(a)–(c). Each raw image is an 8 bit gray value image of $800 \times 800\,\mathrm{px}$. Because of the viewing angle of the camera, the circular shape of the pool's edge is elliptical (red line) in the image. Therefore, a perspective warp to a vertical view of the surface was performed, as shown in figure 3(b), where a large cross indicates the middle point of the surface. Thus, further processing can be performed with fewer perspective disturbances. For the transformation, the points of the primary and secondary diameter of the ellipse are used as reference (red solid circle in figure 3(a)). To transform the ellipse into a circle, the points of the secondary axis are passed to the warp.perspective command of the OpenCv library. From this, the transformation matrix is created and provided to the warp.perspective function to transform the image. The transformation is done without any calibration in this study as only the frequencies of the gray values are evaluated. Structure sizes or lengths are not from interest for the initial measurements and are part of future researches.

The final step of image processing is a polar transformation around the middle point of the surface to reduce the polar coordinates $\phi$ and $r$ to a linear problem in Cartesian coordinates $x$ and $y$, as stated in figure 3(c). The processing of the images allows the detection of surface deformations and wave structures, which can be recognized as differences in the gray values owing to the different light reflections on the

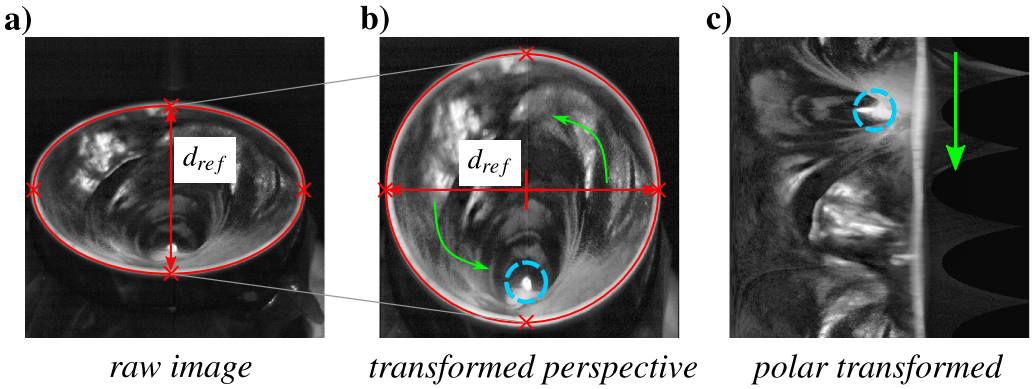


**Figure 3.** (a) Raw image, (b) perspective and (c) polar transformation of the raw image to determine the surface behavior. The red solid lines in (a) and (b) indicate the reference geometry for the image transformation. The green arrows in (b) and (c) indicate the rotation direction or the movement direction on the polar transformed image. The small blue dashed circle in (b) and (c) expresses the change of position between perspective and polar transformation.

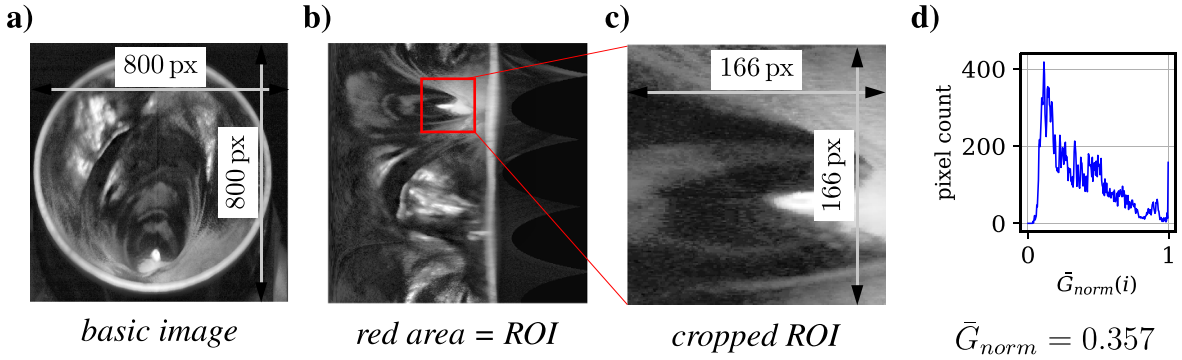


**Figure 4.** Example of the image processing to evaluate the frequency spectra. (a) Raw image, (b) histogram equalized image and marked region of interest (red square), (c) cropped region of interest for gray value estimation, (d) gray value distribution and mean value of the shown example.

curved surface. Due to the polar transformation, it is also easy to distinguish between the radial and circumferential directions of motion of these structures. Please note that the dashed circles in figure 3 just represent the relevant geometry or change in position. The change of the circle sizes has no mean for the actual transformation. The polar-transformed image is then used for data extraction for a fast Fourier transformation (FFT) to obtain the frequency spectra of the surface deformation. All image transformation operations were written in Python source code by using the Opencv 4 computer vision library.

Figures 4(a)–(d) shows the data extraction from the transformed images of the silicon membrane. Following the ideas of [14], we use integral or pseudo integral data from a specific region of interest (ROI) of the surface instead of choosing a point data source for the FFT.

The advantage of the ROI is that the randomness of the position selection, compared to a point source, is minimized. The position of the ROI shown in figure 4(b) was chosen after several preliminary studies.

The next step was to calculate the integral gray value $\bar{G}$ for the ROI. $\bar{G}$ is based on the quotient of the sum of the pixel gray values $G_{\text{pixel}}$ for each image $i$ and the number of all pixels $n_{\text{pixel}}$ in the respective image section

$$\bar{G}(i) = \frac{1}{n_{\text{pixel}}} \sum_{\text{pixel}} G_{\text{pixel}}(i). \tag{2}$$

In addition, the count variable $i$ marks the time $t_i = i \cdot \Delta t$ of the image acquisition. Here, $\Delta t = 1/f_S$ is the time step of the image sampling process.

For the FFT, the pixel standard variation $\sigma(\bar{G})$ and the arithmetic mean value $\bar{G}$ of all evaluated images in a series are used to compute the normalized pixel intensity $\bar{G}_{\text{norm}}$ for each image $i$ using equation (3)

$$\bar{G}_{\text{norm}}(i) = \frac{\bar{G}(i) - \bar{G}}{\sigma(\bar{G})}. \tag{3}$$

This procedure leads to the normalized gray value $\bar{G}_{\text{norm}}$ for the selected example shown in figure 4(d). Then, all gray values $\bar{G}_{\text{norm}}(i)$ of an image series are subjected to FFT analysis. This allows the evaluation of surface motion with respect to high- and low-frequency structures.

The FFT is done with the python function scipy.signal.welch of the scipy library. The function estimates the periodogram of the power spectrum with Welch's method. In general this method splits a given signal $x(t)$ in several

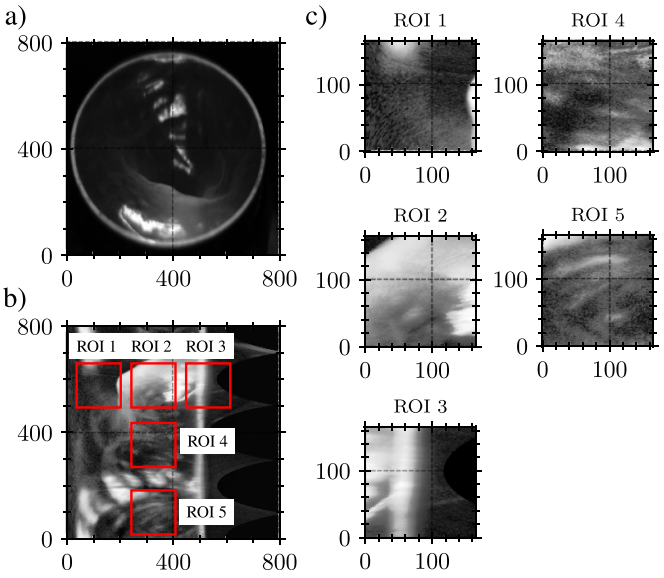


**Figure 5.** (a) Perspective transformed image, (b) transformed image and chosen positions of five ROI for evaluation, (c) cropped image parts of the ROIs.

overlapping parts $x_i(t)$ and performs FFT on these single sequences. Then, the individual periodograms are averaged over time, yielding the final periodogram and power spectrum of the signal $x(t)$. Since our data is imperfect, Welch's method provides a denoising of the data to achieve a clear frequency spectra [15]. The overlap was set to 75 points and the segmentation is set to 1024. To clarify any frequency peaks a Blackman window function is applied to the FFT.

According to Lyons [16], the maximum frequency error $F_{\mathrm{err,max}}$ of the FFT results from the product between the equivalent noise bandwidth of the Blackman window function $B = 1.727$ [16] and the quotient of the segmentation length of the FFT $L_{\mathrm{seg}} = 1024$ and the sampling frequency $F_{\mathrm{S}} = 1000\,\mathrm{Hz}$

$$F_{\mathrm{err,max}} = \frac{1}{2}\frac{F_{\mathrm{S}}}{L_{\mathrm{seg}}}B. \tag{4}$$

For the present work equation (4) yields a maximum frequency error of $F_{\mathrm{err,max}} = 0.843\,\mathrm{Hz}$.

In addition the raw signal is filtered to be able to show the basic trend. The filtering is based on a Savitzky–Golay filter to not completely suppress higher frequency parts of the signal [17]. The filter width was set to 71 time steps $i$ and a weighting function of 3. Please note, that the FFT is done on the normalized raw signal of the measurement.

The integral gray values $\bar{G}$ (see equation (3) and figure 4(b)) for each time step $t$ are assigned over time to produce the plots shown later in figure 8. ROIs were placed at various circumferential and radial locations to test for positional independence. The arrangement was chosen as shown in figure 5. The region where the nozzle can be seen at the low heights $h_{\mathrm{n}}^*$ was not considered. The small preliminary study for $h_{\mathrm{n}}^* = 20$ and $p_0^* = 3$ shows that the signal changes little in the circumferential direction between positions 2, 4, and 5. However, if we change the radial position between 1, 2 and 3, we see that differences in the signal occur due to the proximity to the respective image edges. Thus, the dominant frequencies for ROI 1, 2, and 3 are constant, but for ROI 3 in particular, subthreshold noise can be seen due to the low information content in the edge region. Due to the distinct cavity in the studied configuration, the dominant frequencies can also be determined for ROI 1. But even here, due to the proximity to the edge, image noise can already be detected, which we attribute to the strong distortion caused by the image transformation. For the following evaluations, ROI 2 was therefore taken as a basis, since this is where the focus of the camera is located and thus the information content is highest. The results of this preliminary study for the configuration $h_{\mathrm{n}}^* = 20$ and $p_0^* = 3$ are shown in figure 6. In addition, the size of the ROI was based on the size of the primary structures. The position of the ROI remained constant for all measurement series. In this case, the cavity was selected as the reference size. The ROI is located at the position with the highest information content, that is, the most distinctive gray value differences. Owing to the camera angle and optics, this area is in the foreground of the image.

## 3. Results and discussion

The results of the experiments are discussed starting with a qualitative description of the observations from instantaneous snapshots displayed in figure 7. Subsequently, quantitative results from the image evaluation routines are given in figures 8–10. For clarity of discussion not all results are presented in the following section, but additional results can be found in appendix. In addition to the raw signal the filtered signal is shown in figures 8 and 9 to illustrate the general course. That is, whether the signal is rather afflicted with noise or

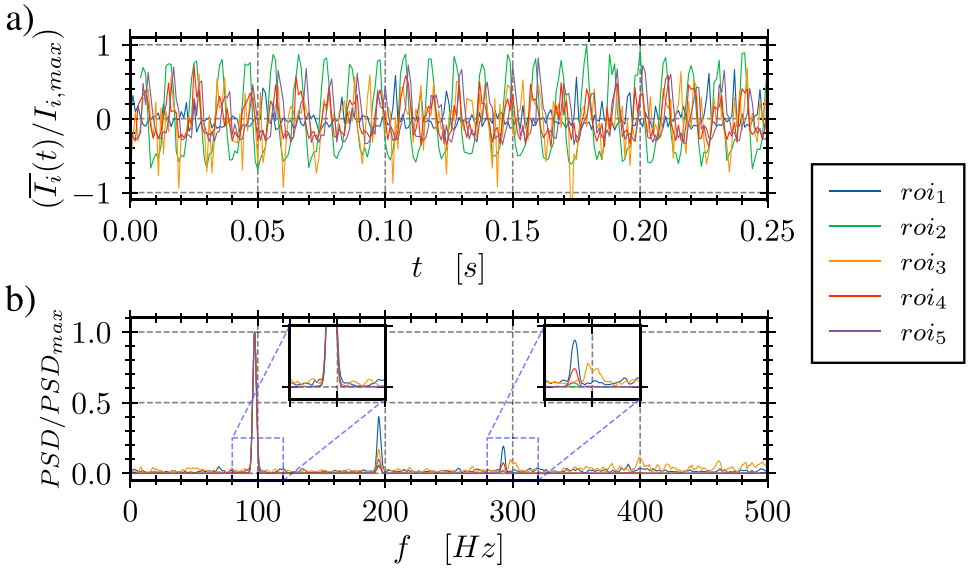


**Figure 6.** Results of the preliminary studies to verify that signals and frequencies are independent of the position for the configuration $h_n^* = 20$ and $p_0^* = 3$. (a) Raw signals of all five ROIs, (b) FFT spectra for all five ROIs.

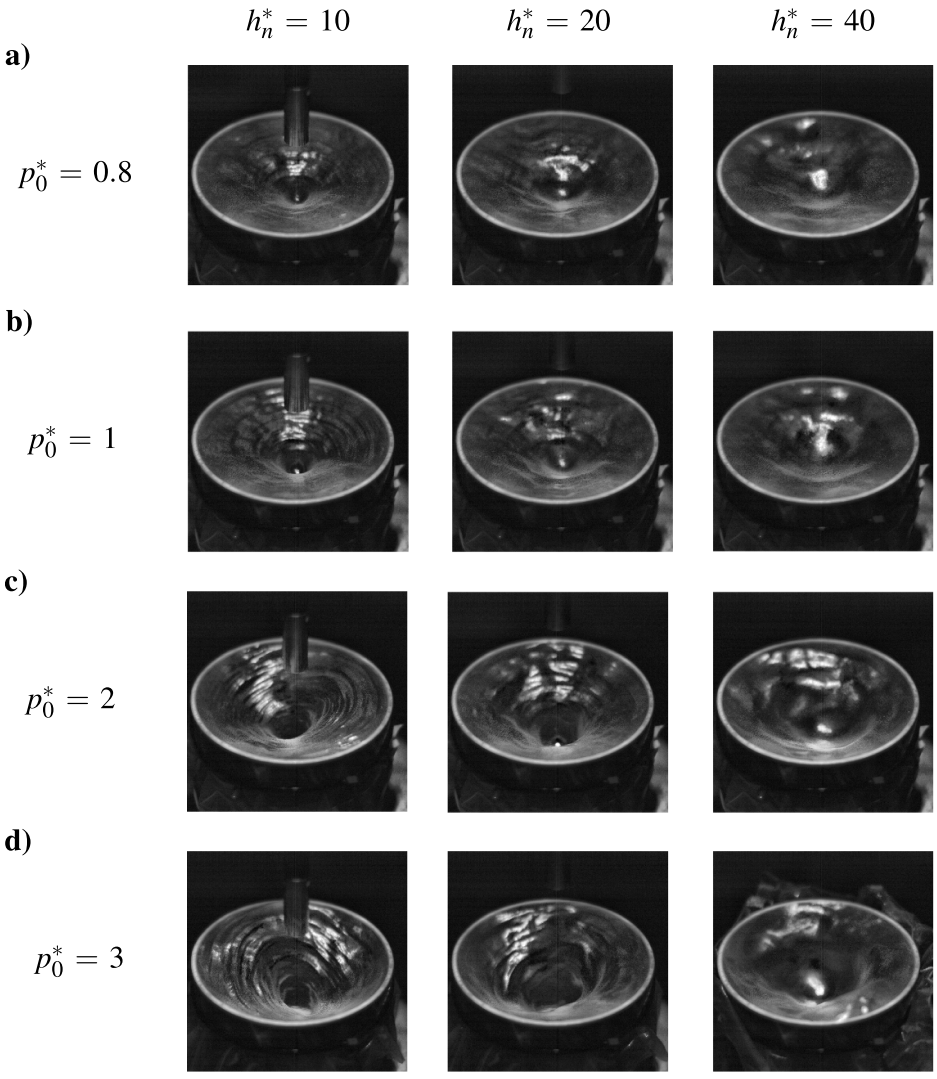


**Figure 7.** Snapshots of the cavity development and surface behavior for all pressure and nozzle heights used in the experiments. The pressures change row wise from (a)–(d) and the nozzle height varies column wise.

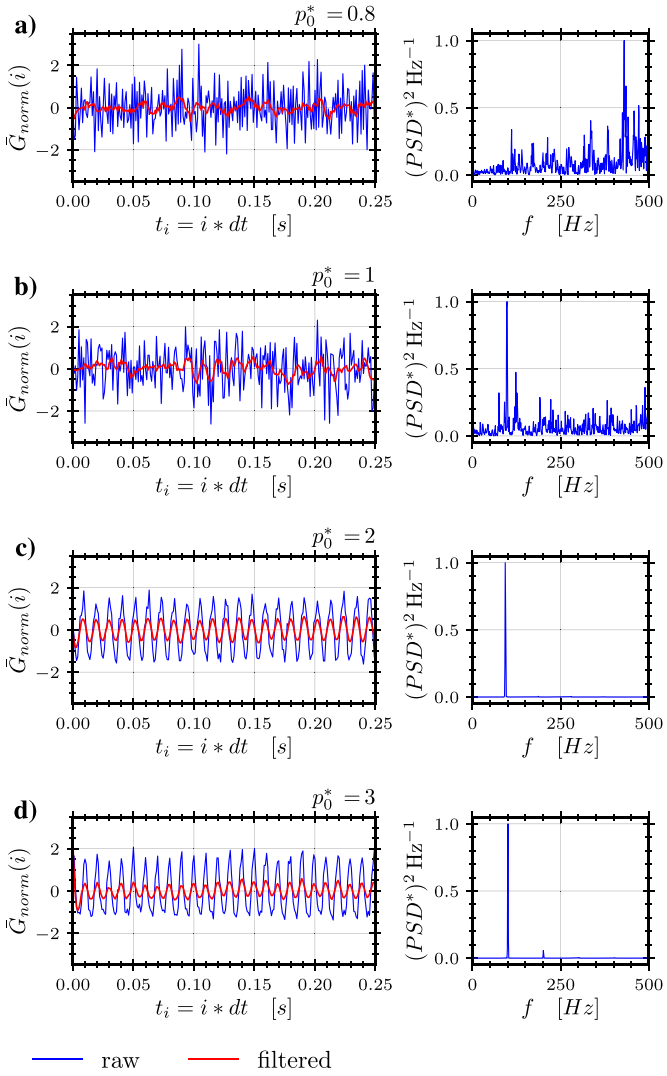


**Figure 8.** Results for $h_n^* = 10$ and all $p_0^*$: (left) plot of the raw signals (blue) and moving averaged (red) and (right) frequency spectra estimated with fast Fourier transformation on the raw signal.

shows a clear trend. Please note that the frequency spectra are based on the raw signal and not on the filtered signal.

The snapshots in figure 7 show representative single images from the different experiments, consisting of 3000 single images, with varying $h_n^*$ and $p_0^*$. In all configurations, the membrane was concavely deformed. In configurations with low $h_n^*$ and/or high $p_0^*$, a deep cavity-like structure was observed in the center of the membrane. This structure was due to the impact of the high-velocity gas jet on the membrane. Small cripple waves were also found in most of these configurations, which were driven by a deflected decelerated jet. Finally, only configurations with low $h_n^*$ and $p_0^*$ values show a nearly axially symmetric membrane image, see e.g. $h_n^* = 10$ and $p_0^* = 0.8$. In contrast, the membrane deformation is asymmetric in configurations with either high values of $h_n^*$ or $p_0^*$, for example $h_n^* = 10$ and $p_0^* = 3$.

Next, all images were processed as described in section 2.2. As an example, sections of the time series $\bar{G}_{\mathrm{norm}}(t_i)$ and corresponding spectra from the FFT of the entire time series are shown in figure 8 for a constant nozzle height $h_n^* = 10$ and varying inlet pressures $p_0^*$. The time series on the left-hand side indicates a transition from irregular, nearly stochastic membrane behavior at $p_0^* = 0.8$ to regular, sinusoidal oscillation of $\bar{G}_{\mathrm{norm}}(t_i)$ at $p_0^* = 3$.

The FFT spectra on the right-hand side of figure 8 provide corresponding information. A broad spectrum without dominant peaks was found at $p_0^* = 0.8$, whereas clear narrow peaks were found at $p_0^* = 3$. Note, that the dominant frequency $f = 100\,\mathrm{Hz}$ is found only in configurations with $p_0^* \geqslant 1$. In configuration $p_0^* = 0.8$, the first noticeable peak is at a slightly higher frequency.

Our interpretation of these findings is as follows. We assume three different regimes of the gas jet/membrane interaction: in regime (i), an axially symmetric gas jet with respect to the nozzle center-line impacts and deforms the membrane. The flow field was in the steady state. The stagnation point of

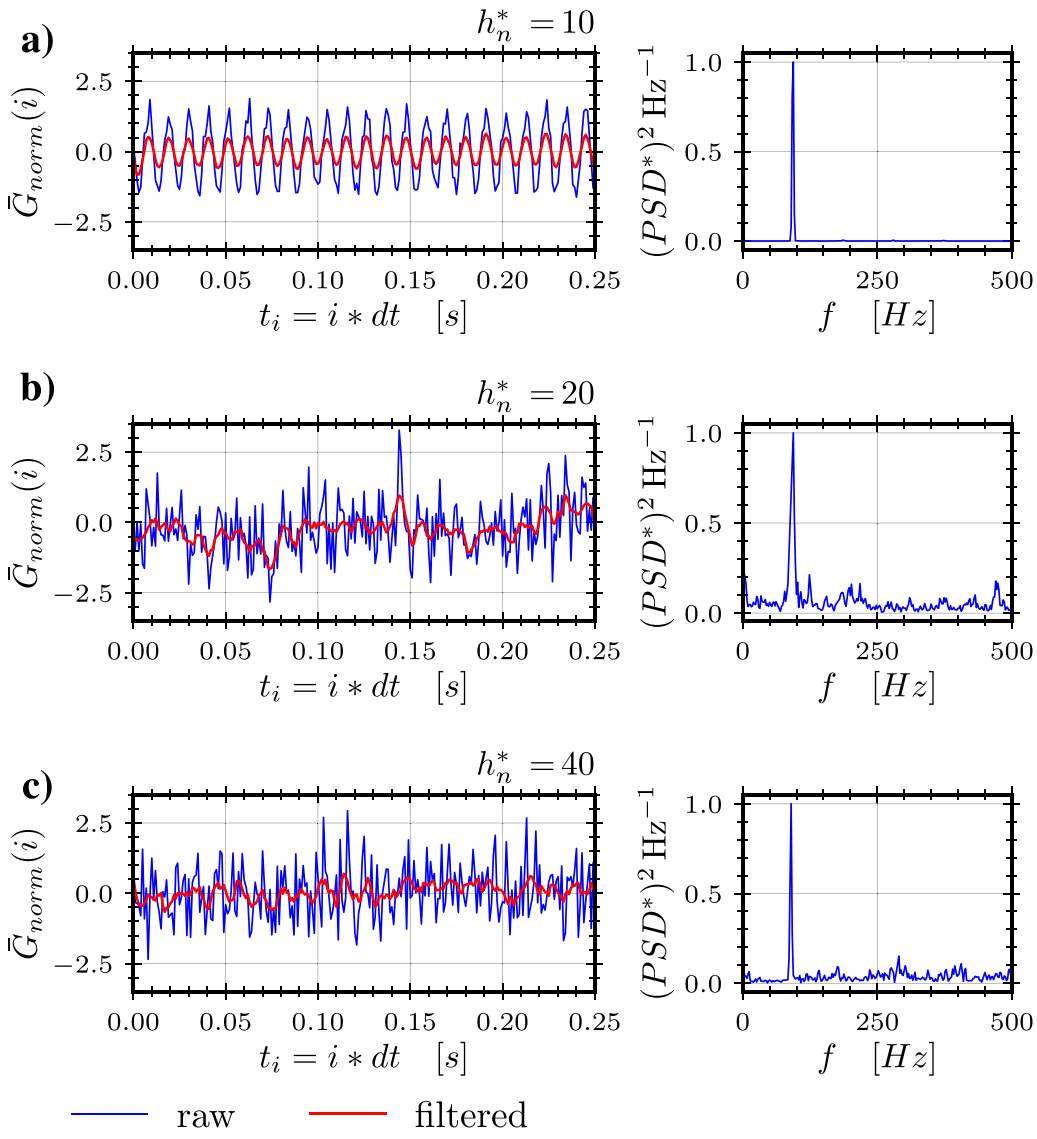


**Figure 9.** Results for $p_0^* = 2$ and $h_n^* = 10$, 20 and 40: (left) plot of the raw signals (blue) and moving averaged (red) and (right) frequency spectra estimated with fast Fourier transformation on the raw signal.

the gas jet induced a deep cavity-like structure. The cripple waves are induced by the jet shear layers that interact with the membrane. These provide a broad frequency spectrum. The configuration $h_n^* = 10$, $p_0^* = 0.8$ is in this regime.

In regime (ii), the gas jet is deflected with respect to the nozzle center-line. Its stagnation point performs a rotational motion with a constant angular velocity along the membrane, a indicated by the rotation of the cavity-like structure. This dominant motion gives a sinusoidal course and clear frequency peaks at $f = 100$ Hz. The cripple waves that are still present are of minor importance in this regime. Configuration ($h_n^* = 10$, $p_0^* = 2$) and ($h_n^* = 10$, $p_0^* = 3$) fall into this regime. Finally, in regime (iii) we observe a marked influence of both the rotational motion of the deep cavity and cripple waves. Configuration ($h_n^* = 10$, $p_0^* = 2$) is an example for this regime.

A similar evaluation of the membrane behavior is shown in figure 9 for configurations with a constant inlet pressure $p_0^* = 2$ but varying nozzle height $h_n^* = 10$. Here, the sections of the time series $\bar{G}_{\mathrm{norm}}(t_i)$ indicate a transition from a regular, sinusoidal oscillating membrane behavior to more irregular membrane deformations with increasing $h_0^*$. However, the FFT spectra indicated, that the membrane behavior was still dominated by the rotational motion of the deep cavity-like structure in these configurations. It should be noted, that the dominant frequency $f = 100$ Hz was found in all these configurations. Therefore, we observed a transition from regime (ii) to regime (iii) with increasing $h_n^*$.

The FFT spectra of all the investigated configurations $h_0^*$, $p_0^*$ are summarized in figure 10. The classification of the investigated configurations into the three different regimes described above is as follows: regime (i) in the upper-left corner (configuration $h_n^* = 10$, $p_0^* = 0.8$), regime (ii) in the lower left part (configurations with $h_n^* = 10$ and/or $p_0^* = 3$) and regime (iii) for all other configurations.

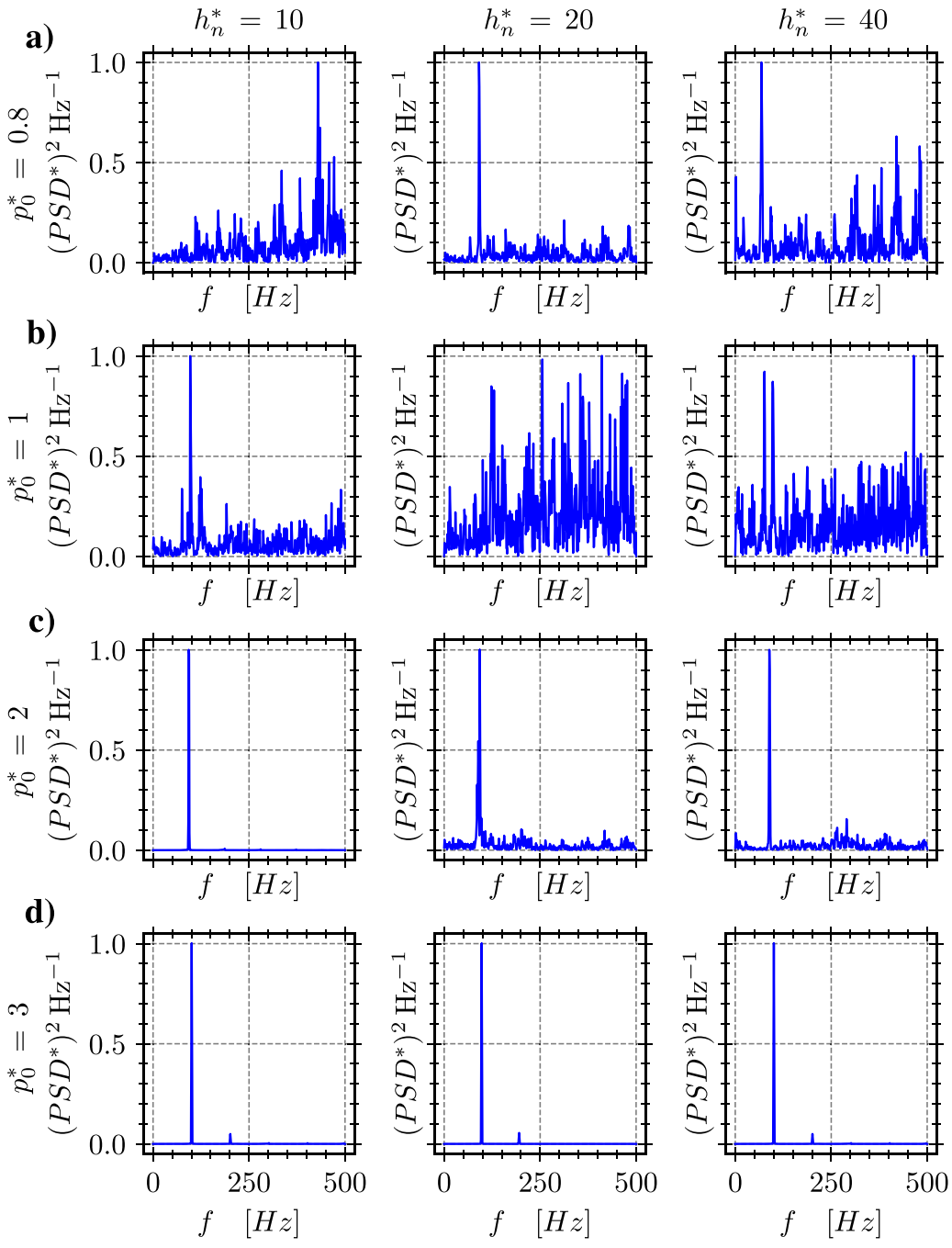


**Figure 10.** Frequency spectra for all investigated configurations of $p_0^*$ and $h_n^*$. The pressures change row wise from (a)–(d) and the nozzle height varies column wise.

To obtain a quantifiable measure for the classification into the different regimes 'axial symmetric/cripple waves', 'angular motion and cripple waves' and 'angular motion' the quantity $P_{\mathrm{mode}}$ is introduced. $P_{\mathrm{mode}}$ is calculated from the quotient $\mathrm{PSD}(h_{\mathrm{n}}^*, p_0^*)_{\mathrm{max}}$ and the root mean square $\mathrm{PSD}(h_{\mathrm{n}}^*, p_0^*)_{\mathrm{rms}}$. Based on this value, the classification can be made as follows: axial symmetric/cripple waves for $P_{\mathrm{mode}} < 10$, angular motion and cripple waves for $10 < P_{\mathrm{mode}} < 15$ and angular motion for $15 < P_{\mathrm{mode}}$.

Figure 11 gives a corresponding mapping of the different regimes in the $h_{\mathrm{n}}^*$-$p_0^*$ space. The mapping shows a clear correlation with the qualitative findings in figure 7. For the lowest value of $h_n^*$ and $p_0^*$ only one point is measured, as it was not possible to measure lower pressures than $p_0^* = 0.8$. Therefore, it is only conditionally possible to assign this configuration to a certain regime, because with the current setup it is not possible to distinguish between surface rotation, symmetric structures or cripple waves as with the other configurations. This point is

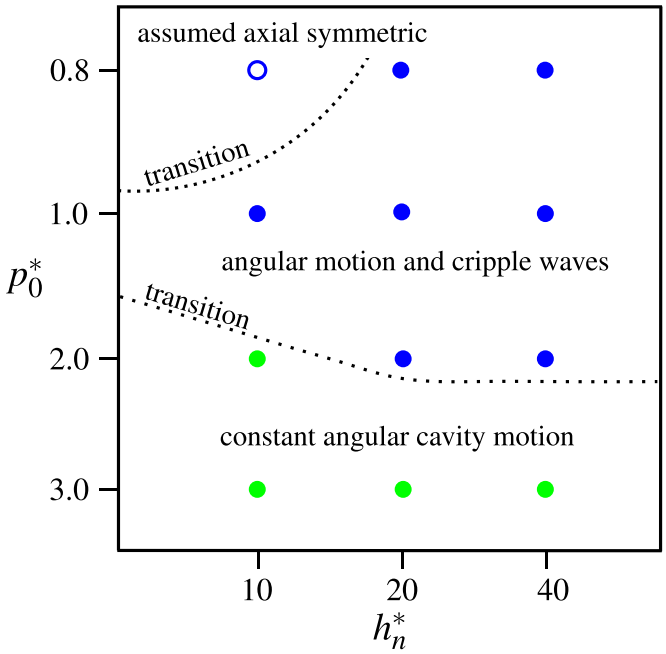


**Figure 11.** Mapping of the different regimes (i)–(iii) in dependence of the parameters $p_0^*$ and $h_n^*$.

therefore marked as a blue circle in figure 11 as the assumed axially symmetric case. Furthermore, it can be assumed that at low pressures the gas jet does not have enough momentum to deform the membrane more than for the combination $p_0^* = 0.8$ and $h_n^* = 10$.

Anyway, we conclude that our new experimental setup enables a detailed qualitative and quantitative investigation of both small-and large-scale surface deformations with broad frequency spectra.

## 4. Summary

A new experimental setup for investigating the interactions between impinging high-speed gas jets and flexible surfaces is introduced. The overall surface behavior was observed from a tilted top view using a high-speed camera. In the present study, a silicon membrane fixed to the edge of an air-filled pool was employed as a flexible surface.

For each gray-value image, a perspective warp to a vertical view of the surface and a transformation into polar coordinates were performed. Surface deformations and wave structures were recognized as differences in the gray values in the images. It was also possible to distinguish between the radial and circumferential direction of motion of these structures. Pseudo-integral data from a specific ROI are used for further quantitative evaluation in the FFT transformations.

Depending on inlet pressure of the Laval nozzle and nozzle-to-surface distance, we observed different deformation regimes of the flexible membrane. With low pressure and distance, an axially symmetric steady-state regime was observed. At high pressure and distance, a constant rotational motion of the dominating surface structure is observed.

The FFT spectra correlate with these qualitative observations. The corresponding mapping of surface behavior is provided in the text. Therefore, it was successfully demonstrated, that the new experimental setup enables detailed qualitative and quantitative investigation of both small- and large-scale surface deformations with broad frequency spectra.

The interactions between the gas-jet and a free liquid surface will be analyzed in the future. However, a more detailed analyses of these interactions requires a more detailed study of the gas flow field, too. Our future research will therefore be based firstly on the interaction between the gas jet and the liquid and secondly on high-speed schlieren images of the gas jet.

## Data availability statement

The data that support the findings of this study are available upon reasonable request from the authors.

## Acknowledgments

Gefördert durch die Deutsche Forschungsgemeinschaft (DFG)- Projektnummer 425860464, funded by the Deutsche Forschungsgemeinschaft (DFG, German Research Foundation)- Projektnummer 425860464.

The authors also thank Kevin Schulze from our mechanical workshop for helpful discussions regarding the manufacturing of the test rig and Lukas Jung for supporting the measurements.

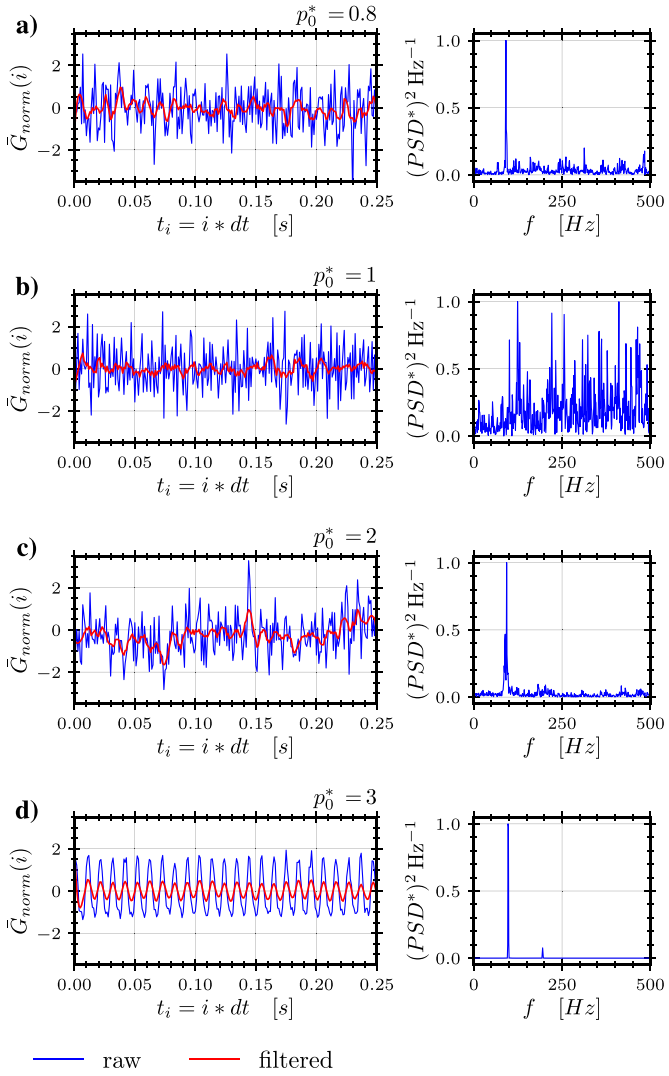


**Figure 12.** Results for $20h_n/D_n$: plot of the raw signals (blue) and moving averaged (red) and frequency spectra estimated with fast Fourier transformation.

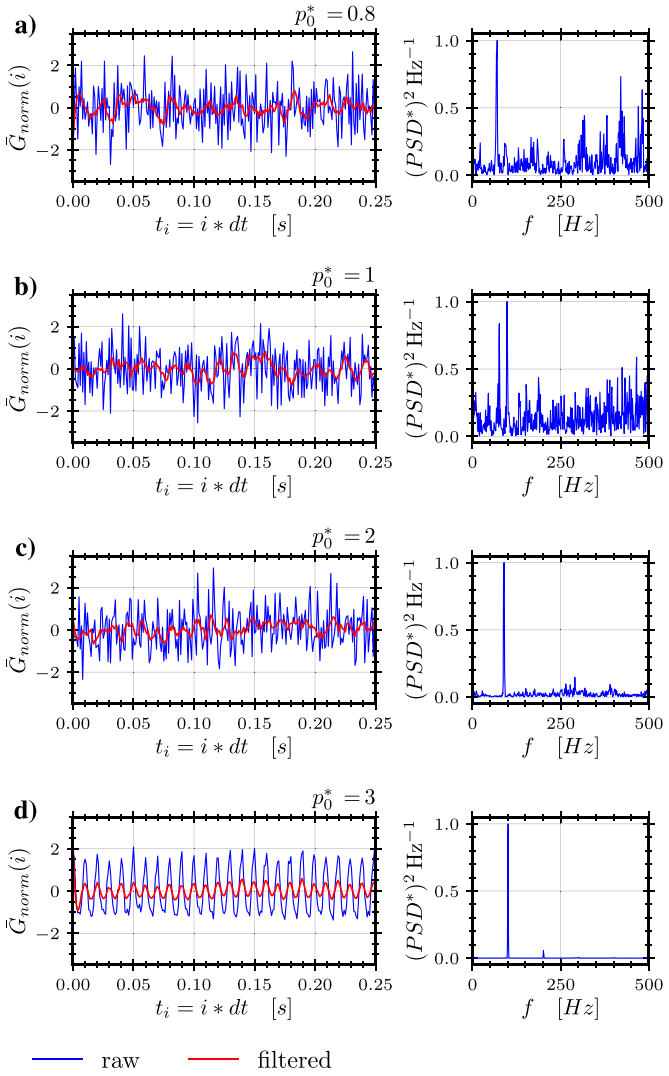


**Figure 13.** Results for $40h_n/D_n$: plot of the raw signals (blue) and moving averaged (red) and frequency spectra estimated with fast Fourier transformation.

## Appendix

The appendix contains the FFT results for $h*_{20}$ and 40, as shown in figures 12 and 13. Overall, the same trends of the signals were observed for the foregoing results. However, a closer look shows that there is a slight difference in the raw signals for a lower $p_0^*$. The raw signal is a mix of short and long-period events, as indicated by the FFT. As figure 7 shows, the cavity is flat and broad, and the surface is speckled with small structures of high frequency, but also larger wave-like formations are visible at the same time. For $p_0^* = 1$, the same cavity evolution and surface structures were apparent. Owing to the greater impact of the gas jet a shift to low-frequency events occurred in the FFT spectra. For $p_0^* = 2$ and $p_0^* = 3$ the frequency range again yields a shift to low frequency events with a slight influence of high frequency patterns. We assume that the still existing swirl of the surface is the offspring of the low-frequency peaks, even for the higher values of $h_n^*$ as the time-resolved image series exposure.

## ORCID iD

Johannes Burkert https://orcid.org/0000-0002-2573-5842

## References

[1] Mitchell D M, Honnery D R and Soria J 2012 The visualization of the acoustic feedback loop in impinging underexpanded supersonic jet flows using ultra-high frame rate schlieren *J. Vis.* **15** 333–41

[2] Dhamanekar A and Srinivasan K 2018 Mitigation of impinging tones using central protrusion *J. Sound Vib.* **433** 160–78

[3] Edgington-Mitchell D 2019 Aeroacoustic resonance and self-excitation in screeching and impinging supersonic jets—a review *Int. J. Aeroacoust.* **18** 118–88

[4] Davis T, Edstrand A, Alvi F, Cattafesta L, Yorita D and Asai K 2015 Investigation of impinging jet resonant modes using unsteady pressure-sensitive paint measurements *Exp. Fluids* **56** 1–13

[5] Li M, Li Q, Zou Z and Li B 2019 Characterization of cavity oscillation and splashing distribution under excitation by

bottom gas blowing in a steelmaking converter *JOM* **71** 729–36
[6] Mendez M A, Gosset A and Buchlin J-M 2019 Experimental analysis of the stability of the jet wiping process, part II: multiscale modal analysis of the gas jet-liquid film interaction *Exp. Therm. Fluid Sci.* **106** 48–67
[7] Page G J, Li Q and McGuirk J J 2005 LES of impinging jet flows relevant to vertical landing aircraft *23rd AIAA Applied Aerodynamics Conf.* vol 2 pp 1365–76
[8] Kondeti V S S K and Bruggeman P J 2021 The interaction of an atmospheric pressure plasma jet with liquid water: dimple dynamics and its impact on crystal violet decomposition *J. Phys. D: Appl. Phys.* **54** 045204
[9] Banks R B and Chandrasekhara D V 1963 Experimental investigation of the penetration of a high-velocity gas jet through a liquid surface *J. Fluid Mech.* **15** 13–34
[10] Asahara N, Naito K-I, Kitagawa I, Matsuo M, Kumakura M and Iwasaki M 2011 Fundamental study on interaction between top blown jet and liquid bath *Steel Res. Int.* **82** 587–94
[11] Hwang H Y and Irons G A 2012 A water model study of impinging gas jets on liquid surfaces *Metall. Mater. Trans.* B **43** 302–15
[12] Ek M and Sichen D 2012 Study of penetration depth and droplet behavior in the case of a gas jet impinging on the surface of molten metal using liquid Ga–In–Sn *Steel Res. Int.* **83** 678–85
[13] Molloy N 1970 Impinging jet flow in a two-phase system. The basic flow pattern *J. Iron Steel Inst.* **208** 943–50
[14] Wang Z, Örlü R, Schlatter P and Chung Y M 2018 Direct numerical simulation of a turbulent 90° bend pipe flow *Int. J. Heat Fluid Flow* **73** 199–208
[15] Welch P 1967 The use of fast Fourier transform for the estimation of power spectra: a method based on time averaging over short, modified periodograms *IEEE Trans. Audio Electroacoust.* **15** 70–73
[16] Lyons R G 2004 *Understanding Digital Signal Processing* 2nd edn (Upper Saddle River, NJ: Pearson Education)
[17] Savitzky A and Golay M J E 1964 Smoothing and differentiation of data by simplified least squares procedures *Anal. Chem.* **36** 1627–39